Auger spectrum of a water molecule after single and double core ionization

L. Inhester, C. F. Burmeister, G. Groenhof, and H. Grubmüller

Additional information on J. Chem. Phys.

Auger spectrum of a water molecule after single and double core ionization

L. Inhester,[a)] C. F. Burmeister, G. Groenhof, and H. Grubmüller

Max Planck Institute for Biophysical Chemistry, Am Faßberg 11, 37077 Göttingen, Germany

The high intensity of free electron lasers opens up the possibility to perform single-shot molecule scattering experiments. However, even for small molecules, radiation damage induced by absorption of high intense x-ray radiation is not yet fully understood. One of the striking effects which occurs under intense x-ray illumination is the creation of double core ionized molecules in considerable quantity. To provide insight into this process, we have studied the dynamics of water molecules in single and double core ionized states by means of electronic transition rate calculations and *ab initio* molecular dynamics (MD) simulations. From the MD trajectories, photoionization and Auger transition rates were computed based on electronic continuum wavefunctions obtained by explicit integration of the coupled radial Schrödinger equations. These rates served to solve the master equations for the populations of the relevant electronic states. To account for the nuclear dynamics during the core hole lifetime, the calculated electron emission spectra for different molecular geometries were incoherently accumulated according to the obtained time-dependent populations, thus neglecting possible interference effects between different decay pathways. We find that, in contrast to the single core ionized water molecule, the nuclear dynamics for the double core ionized water molecule during the core hole lifetime leaves a clear fingerprint in the resulting electron emission spectra. The lifetime of the double core ionized water was found to be significantly shorter than half of the single core hole lifetime. © *2012 American Institute of Physics*. [http://dx.doi.org/10.1063/1.3700233]

I. INTRODUCTION

Ultra intense femtosecond free electron lasers (FEL) allow one to study several new phenomena in molecules and atoms and hold the promise to obtain x-ray scattering information from large biomolecules such as proteins at the single molecule level.[1,2] Molecules exposed to intense x-ray pulses are expected to undergo severe radiation damage.[1] At illumination conditions in the x-ray regime the dominant electronic process is photoionization of core electrons into the continuum. These core ionizations trigger autoionization processes, e.g., Auger decay, which cause refilling of the core hole vacancy while emitting a secondary electron that carries away the excess energy.

Recent theoretical studies have addressed the formation of multiple core ionized electronic states by x-ray FEL radiation in atoms.[3–5] These electronic states mainly result from sequential photoionization processes where the second photoionization occurs faster than the refilling of the core shell by Auger decay. Double core hole states are of particular interest in spectroscopy, as they can provide more insight into molecular structure than conventional single core spectroscopy.[6–9] In experiments with intense FEL x-ray pulses at the Linac Coherent Light Source (LCLS) significant quantities of such multiple core ionized states in neon atoms[10] and nitrogen molecules[11] were observed.

In addition to the pure electronic radiation damage, a second consequence of the exposure of molecules to intense x-ray radiation is the fast dissociative motion, the so-called Coulomb explosion, which is triggered by the fast charging of the molecule. This process has been studied by molecular dynamics force field simulations,[1,12–14] in which electronic transitions are described stochastically, governed by atomic transition rates. However, because the molecular dynamics strongly depends on the ionization kinetics, accurate molecular photoionization, and Auger decay rates are desirable. From another point of view, Auger spectroscopy may provide a means to study the ionization dynamics and might give information on the fast nuclear motion. It is therefore of interest to elucidate ionization of molecules by intense x-ray radiation and the formation of the corresponding Auger spectra with respect to the several ionization steps and the rapid nuclear motion.

One of the main challenges of calculating molecular Auger decay rates is the appropriate description of the continuum electron wavefunction, which cannot be represented by the commonly used square-integrable (L^2) basis functions. Auger transitions for small molecules have been studied in several approaches, using (i) Stieltjes imaging,[15] (ii) solving the Lippmann-Schwinger equation on a basis of Gaussian-type functions,[16,17] (iii) the so-called *one-center approach* using atomic radial Auger integrals,[18] and (iv) based on population analysis.[19,20] The former two approaches rely on an asymptotical description of the continuum wavefunction with Gaussian basis functions close to the molecule, whereas the one-center approach uses atomic continuum wavefunctions. The method based on population analysis does not include the continuum electron explicitly.

_____
a)linhest@gwdg.de.

Here, we calculated molecular ionization and Auger transition rates using the *single center expansion* (SCE) method.[21] In our approach the continuum wavefunction is obtained by explicit integration of a set of coupled (static) radial Schrödinger equations, whereas the remaining bound electrons are described by usual linear combination of atomic orbitals (LCAO). This hybrid approach enabled us to accurately represent continuum wave functions while taking advantage of efficient L^2 basis sets for the bound orbitals.

Using the obtained molecular ionization and Auger decay rates, time-dependent populations of the single and double core ionized states were calculated, similarly to previous approaches for atoms.[3–5] To also include effects of nuclear motion on the Auger spectrum within the core hole life time, we *incoherently* summed up instantaneous Auger spectra for different molecular geometries, obtained by classically propagating the nuclei positions with forces calculated "on the fly" for the core ionized electronic states. Such approach, already applied in previous calculations,[22,23] avoids the explicit computation of the many involved potential energy surfaces but neglects possible interference effects on the spectrum. Other approaches, which address effects of nuclear motion in a coherent way and, thereby, are able to address vibrational features of the spectrum, rely on pre-calculated potential energy surfaces. For examples, Eroms *et al.*[24] used the multi-configurational time-dependent Hartree technique to propagate the nuclear wave packets for the resonant Auger spectrum of water. Bao *et al.*[25] presented a calculation of the normal Auger spectrum of the oxygen molecule based on the Kramers-Heisenberg formula.

As a model system we considered the Auger spectrum of a singly and doubly core ionized water molecule. While the single core Auger spectrum ($K - LL$) of water has been extensively studied,[15,23,26] we are not aware of any studies of its double core Auger spectra ($KK - KLL$). Our results confirm that the nuclear motion has little effect on the Auger spectrum during the few femtoseconds of the core hole lifetime for single core ionized water.[23] Strikingly, however, the nuclear motion of double core ionized water was found to markedly affect the Auger spectrum due to fast dissociation dynamics.

The outline of the paper is as follows. Our approach to determine ionization transition rates is described in Sec. II. Section III describes the computational details of the calculations. Results and conclusion are presented in Secs. IV and V.

II. CALCULATION OF ELECTRONIC IONIZATION TRANSITIONS RATES

Calculation of ionization rates requires the description of initial $|\psi_{\text{ini}}\rangle$ and final $|\psi_{\text{fin}}\rangle$ electronic wave functions. To clarify the notation, we first describe in Subsection II A how the final electronic states $|\psi_{\text{fin}}\rangle$ are constructed from a molecular bound part and a continuum part. In Subsections II B and II C we describe how photoionization cross sections and Auger decay rates are obtained.

A. Construction of the final electronic state

A total final electronic state $|\psi_{\text{fin}}\rangle$ after ionization is constructed by combining a multi-electron bound part $|\tilde{\psi}_{\text{fin}}\rangle$ and a single electron part described by the continuum electron wave function $\phi_{k,\sigma}(\mathbf{r})$ with energy $\epsilon = k^2/2$ and spin σ. Following spin addition rules[27] the state is given by

$$|\psi_{\text{fin},M_S=1/2}^{(1)S=1/2}\rangle = c_{k,\alpha}^\dagger |\tilde{\psi}_{\text{fin},M_S=0}^{S=0}\rangle, \tag{1}$$

$$|\psi_{\text{fin},M_S=1/2}^{(2)S=1/2}\rangle = \frac{1}{\sqrt{3}}\left(-c_{k,\alpha}^\dagger |\tilde{\psi}_{\text{fin},M_S=0}^{S=1}\rangle + \sqrt{2}c_{k,\beta}^\dagger |\tilde{\psi}_{\text{fin},M_S=1}^{S=1}\rangle\right), \tag{2}$$

for doublet states and

$$|\psi_{\text{fin},M_S=0}^{S=0}\rangle = \frac{1}{\sqrt{2}}\left(-c_{k,\alpha}^\dagger |\tilde{\psi}_{\text{fin},M_S=-1/2}^{S=1/2}\rangle + c_{k,\beta}^\dagger |\tilde{\psi}_{\text{fin},M_S=1/2}^{S=1/2}\rangle\right), \tag{3}$$

for singlet states. The additional indices S and M_S describe total spin quantum numbers[28] and $c_{k,\sigma}^\dagger$ is the creation operator for a continuum electron with wavefunction $\phi_{k,\sigma}(\mathbf{r})$.

For the evaluation of transition rates given by first-order perturbation theory, matrix elements of an operator O between initial $|\psi_{\text{ini},M_S}^S\rangle$ and final states $|\psi_{\text{fin},M_S}^S\rangle$ have to be calculated. Assuming O commutes with spin S, expressions for final states $|\psi_{\text{fin},M_S=1/2}^{(2)S=1/2}\rangle$ and $|\psi_{\text{fin},M_S=0}^{S=0}\rangle$ can be simplified to[29]

$$\left|\langle\psi_{\text{ini},M_S=1/2}^{S=1/2}|O|\psi_{\text{fin},M_S=1/2}^{(2)S=1/2}\rangle\right|^2$$
$$= 3\left|\langle\psi_{\text{ini},M_S=1/2}^{S=1/2}|O|c_{k,\alpha}^\dagger\tilde{\psi}_{\text{fin},M_S=0}^{S=1}\rangle\right|^2, \tag{4}$$

$$\left|\langle\psi_{\text{ini},M_S=0}^{S=0}|O|\psi_{\text{fin},M_S=0}^{S=0}\rangle\right|^2$$
$$= 2\left|\langle\psi_{\text{ini},M_S=0}^{S=0}|O|c_{k,\alpha}^\dagger\tilde{\psi}_{\text{fin},M_S=-1/2}^{S=1/2}\rangle\right|^2. \tag{5}$$

The bound part $|\tilde{\psi}_{\text{fin},M_S}^S\rangle$ of the final electronic wavefunction can be represented by the usual linear combination of atomic orbitals (LCAO), while the description of the continuum wavefunction $\phi_{k,\sigma}$ requires a continuum representation. Here we represent $\phi_{k,\sigma}$ in a single center expansion[21] given by

$$\phi_{k,\sigma}(\mathbf{r}) = \sum_{lm} \frac{P_{lm}^k(r)}{r} Y_{lm}(\theta,\phi), \tag{6}$$

where $Y_{lm}(\theta,\phi)$ are spherical harmonics, and the $P_{lm}^k(r)$ are a set of radial wave functions, which solve the set of coupled radial Schrödinger equations[21]

$$\frac{d^2}{dr^2}P_{lm}^k(r) + \sum_{l'm'} M_{lm,l'm'}(r)P_{l'm'}^k(r) = 0, \tag{7}$$

with

$$M_{lm,l'm'}(r) := \delta_{l',l}\delta_{m',m}\left(\frac{-l(l+1)}{r^2} + 2\epsilon\right)$$
$$+ 2\sum_{l''m''} v_{l''m''}(r)\int d\Omega\, Y_{lm}^*(\theta,\phi)$$
$$\times Y_{l''m''}(\theta,\phi)Y_{l'm'}(\theta,\phi). \qquad (8)$$

Here, $\int d\Omega$ describes integration over the solid angle and $v_{lm}(r)$ are the radial parts of the SCE of the potential $V(\mathbf{r})$, where

$$V(\mathbf{r}) = \sum_{lm}\frac{v_{lm}(r)}{r}Y_{lm}(\theta,\phi) = V_{\text{ne}}(\mathbf{r}) + V_{\text{ee}}(\mathbf{r})$$
$$= \sum_{lm}\frac{v_{lm}^{ne}(r) + v_{lm}^{ee}(r)}{r}Y_{lm}(\theta,\phi). \qquad (9)$$

$V_{\text{ne}}(\mathbf{r})$ is the nuclear potential of the molecule and $V_{\text{ee}}(\mathbf{r})$ represents the interaction of the continuum electron with the remaining bound electrons. For the spherical nuclear coordinates R_n, θ_n, ϕ_n of nucleus $n = 1\dots N$, the radial parts $v_{lm}^{ne}(r)$ of the nuclear potential are given by

$$v_{lm}^{ne}(r) = \sum_n -Z_n r\frac{r_<^l}{r_>^{l+1}}Y_{lm}^*(\theta_n,\phi_n), \qquad (10)$$

with $r_< = \min(r, R_n)$ and $r_> = \max(r, R_n)$ and Z_n being the charge of nucleus n. The electron-electron interaction $V_{\text{ee}}(\mathbf{r})$ is determined by the electrostatic potential of the charge density $\tilde{\rho}(\mathbf{r})$ of the electrons in the bound part $|\tilde{\psi}_{\text{fin}}\rangle$,

$$J(\mathbf{r}) = \int d\mathbf{r}'\frac{\tilde{\rho}(\mathbf{r}')}{|\mathbf{r} - \mathbf{r}'|}, \qquad (11)$$

and the shorter ranged exchange part. We used the KSG (Ref. 30) exchange potential,

$$V_{\text{XC}}[\tilde{\rho}(\mathbf{r})] = -\left(\frac{3}{\pi}\tilde{\rho}(\mathbf{r})\right)^{\frac{1}{3}}, \qquad (12)$$

to model the exchange interaction, which renders Eq. (7) as a homogenous differential equation. To further simplify the calculations, the non-spherical symmetric parts ($l \neq 0$) of the electron density $\tilde{\rho}(\mathbf{r})$ in the exchange potential (Eq. (12)) are approximated by first-order Taylor expansion

$$V_{\text{XC}}[\tilde{\rho}(\mathbf{r})] = -\left(\frac{3}{\pi}\frac{\tilde{\rho}_{00}(r)}{r}Y_{00}\right)^{\frac{1}{3}}\left[1 + \frac{1}{3}\sum_{l\neq 0,m}\frac{\tilde{\rho}_{lm}(r)Y_{lm}(\theta,\phi)}{\tilde{\rho}_{00}(r)Y_{00}}\right.$$
$$\left. + \mathcal{O}\left(\sum_{l\neq 0,m}\frac{\tilde{\rho}_{lm}(r)Y_{lm}(\theta,\phi)}{\tilde{\rho}_{00}(r)Y_{00}}\right)^2\right], \qquad (13)$$

where $\tilde{\rho}_{lm}(r)$ are the radial parts of the SCE of the electron density

$$\tilde{\rho}(\mathbf{r}) = \sum_{lm}\frac{\tilde{\rho}_{lm}(r)}{r}Y_{lm}(\theta,\phi). \qquad (14)$$

The radial parts $v_{lm}^{ee}(r)$ of the electron-electron interactions in Eq. (9) are finally given by the SCE of Coulomb potential $J(\mathbf{r})$

and the electron density $\tilde{\rho}(\mathbf{r})$,

$$r \cdot v_{lm}^{ee}(r) \simeq \int d\Omega\, Y_{lm}^*(\theta,\phi)J(\mathbf{r}) + \frac{-1}{Y_{00}}\left(\frac{3}{\pi}\frac{\tilde{\rho}_{00}(r)}{r}Y_{00}\right)^{\frac{1}{3}}$$
$$\times \begin{cases} 1 & \text{for } l = 0 \\ \tilde{\rho}_{lm}(r)/(3\tilde{\rho}_{00}(r)) & \text{else.} \end{cases} \qquad (15)$$

Subsequently, the energy-degenerated solutions of Eq. (7), $P_{lm}^{\prime k,LM}(r)$, are labeled by the additional index tuple LM. They are required to fulfill the boundary conditions

$$P_{lm}^{\prime k,LM}(r \to 0) = 0, \qquad (16)$$

$$P_{lm}^{\prime k,LM}(r \to \infty) = \sqrt{\frac{2}{\pi k}}(\delta_{LM,lm}F_l(kr) + R_{LM,lm}\,G_l(kr)). \qquad (17)$$

$F_l(kr)$ and $G_l(kr)$ are the regular and irregular Coulomb functions and $R_{LM,lm}$ are elements of an hermitian matrix $\mathbf{R}$ determined by the asymptotic behavior of the solutions.[21]

The above mentioned boundary conditions do not provide an energy-normalized solution, as required for correct transition rates. Hence, energy normalization is achieved by the linear combination[31]

$$P_{lm}^{k,LM}(r) = \sum_{L'M'}\frac{1}{\sqrt{1 + \lambda_{LM}}}U_{LM,L'M'}P_{lm}^{\prime k,L'M'}, \qquad (18)$$

where the columns of $\mathbf{U}$ and λ_{LM} are eigenvectors and eigenvalues of the Matrix $\mathbf{R}$, respectively.

Note, that here the bound electrons are considered to be not affected by the continuum electron, thus the bound electron part can be calculated independently. To evaluate electronic transition rates, electron integrals between bound and continuum electrons have to be calculated. For the purpose of calculating these quantities within the SCE, also the bound orbitals are expanded into the SCE as in Eq. (6).

B. Photoionization

Following first-order perturbation theory, the photoionization cross sections $\sigma_{\text{ini}\to\text{fin}}$ in length gauge is proportional to the dipole matrix elements between the initial $|\psi_{\text{ini}}\rangle$ and final $|\psi_{\text{fin}}\rangle$ electronic states,[32]

$$\sigma_{\text{ini}\to\text{fin}} = 4\alpha\pi^2\omega|\langle\psi_{\text{ini}}|\mathbf{s}\cdot\mathbf{d}|\psi_{\text{fin}}\rangle|^2, \qquad (19)$$

where $\alpha \simeq 1/137$ is the fine-structure constant, ω is the photon energy, and $\mathbf{s}$ is the electric polarization vector of the electromagnetic wave. The elements of the transition dipole moment $\mathbf{d}$ are expressed in the SCE by[5]

$$d_M = c_i^\dagger c_j\sqrt{\frac{4\pi}{3}}\sum_{lml'm'}\int_0^\infty dr\, P_{lm}^{i*}(r)r P_{l'm'}^{j}(r)$$
$$\times \int d\Omega\, Y_{lm}(\theta,\phi)Y_{l'm'}^*(\theta,\phi)Y_{1M}^*(\theta,\phi), \qquad (20)$$

where $P_{lm}^i(r)$ and $P_{l'm'}^j(r)$ represent radial parts of the respective bound and continuum electron wave functions and $c_i^\dagger$, c_j

are the corresponding creation/annihilation operators, respectively. Averaging over all molecular orientations, yields

$$\sigma_{\text{ini}\to\text{fin}} = \frac{4}{3}\alpha\pi^2\omega \sum_{M=-1,0,1} |\langle\psi_{\text{ini}}|d_M|\psi_{\text{fin}}\rangle|^2. \quad (21)$$

The photoionization transition rate is given by

$$\Gamma^{\text{Photo}}_{\text{ini}\to\text{fin}} = \sigma_{\text{ini}\to\text{fin}} \cdot F(t), \quad (22)$$

where $F(t)$ is the time-dependent photon flux. The total photoionization cross section σ_{ini} reads

$$\sigma_{\text{ini}} = \sum_{\text{fin}} \sigma_{\text{ini}\to\text{fin}}. \quad (23)$$

The above summation involves different continuum solutions (LM) as well as different electronic bound parts ($|\tilde\psi_{\text{fin}}\rangle$).

C. Auger transition

The transition rate for Auger decay $\Gamma^{\text{Auger}}_{\text{ini}\to\text{fin}}$ from first-order perturbation theory is given by

$$\Gamma^{\text{Auger}}_{\text{ini}\to\text{fin}} = 2\pi |\langle\psi_{\text{fin}}|H - E_{\text{ini}}|\psi_{\text{ini}}\rangle|^2. \quad (24)$$

Assuming vanishing state overlap $\langle\psi_{\text{fin}}|\psi_{\text{ini}}\rangle = 0$, the Auger transition rates are given by matrix elements of the electronic Hamiltonian,[33]

$$\langle\psi_{\text{fin}}|H - E_{\text{ini}}|\psi_{\text{ini}}\rangle$$

$$= \langle\psi_{\text{fin}}| \left(\sum_{ij} c_i^\dagger c_j h_{ij} + \frac{1}{2}\sum_{ijkl} c_i^\dagger c_j^\dagger c_l c_k \langle ij|kl\rangle \right) |\psi_{\text{ini}}\rangle. \quad (25)$$

The above two- and one-electron integrals are readily evaluated in the SCE representation,

$$h_{ij} = \delta_{\sigma_i,\sigma_j} \int d\mathbf{r}\,\phi_i^*(\mathbf{r}) \left(-\frac{\Delta}{2} + V_{ne}(\mathbf{r}) \right) \phi_j(\mathbf{r})$$

$$= \delta_{\sigma_i,\sigma_j} \int_0^\infty dr \left(\sum_{lm} \frac{1}{2} \frac{dP_{lm}^{i*}(r)}{dr} \frac{dP_{lm}^j(r)}{dr} \right.$$

$$+ \sum_{\substack{lm \\ l'm'l''m''}} \frac{P_{lm}^{i*}(r) v_{ne,l'm'}(r) P_{l''m''}^j(r)}{r}$$

$$\left. \times \int d\Omega\, Y_{lm}^*(\theta,\phi) Y_{l'm'}(\theta,\phi) Y_{l''m''}(\theta,\phi) \right), \quad (26)$$

and

$$\langle ij|kl\rangle := \delta_{\sigma_i,\sigma_k}\delta_{\sigma_j,\sigma_l}(ik|jl), \quad (27)$$

$$(ik|jl) = \int d^3r_1 \int d^3r_2\, \phi_i^*(\mathbf{r_1})\phi_k(\mathbf{r_1}) \frac{1}{r_{12}} \phi_j^*(\mathbf{r_2})\phi_l(\mathbf{r_2})$$

$$= \sum_{\substack{lm \\ l'm'l''m''}} \int_0^\infty dr\, y_{lm}^{ik}(r) P_{l'm'}^{j*}(r) P_{l''m''}^l(r)$$

$$\times \int d\Omega\, Y_{lm}^*(\theta,\phi) Y_{l'm'}^*(\theta,\phi) Y_{l''m''}(\theta,\phi), \quad (28)$$

$$y_{lm}^{ik}(r) := \sum_{\substack{l'm' \\ l''m''}} \int_0^\infty dr' \frac{4\pi P_{l'm'}^{i*}(r) P_{l''m''}^k(r)}{2l+1} \frac{r_<^l}{r_>^{l+1}}$$

$$\times \int d\Omega\, Y_{lm}(\theta,\phi) Y_{l'm'}^*(\theta,\phi) Y_{l''m''}(\theta,\phi). \quad (29)$$

Here, σ_i is the spin of spin orbital ϕ_{i,σ_i}, $r_< = \min(r, r')$ and $r_> = \max(r, r')$. Neglecting other relaxation effects such as fluorescence—which is small for the light nuclei considered here—the total lifetime τ of the initial state is given by

$$\tau = 1/\Gamma^{\text{Auger}}_{\text{ini}} = 1/\sum_{\text{fin}} \Gamma^{\text{Auger}}_{\text{ini}\to\text{fin}}, \quad (30)$$

where $\Gamma^{\text{Auger}}_{\text{ini}}$ is the total transition rate of the initial state. Again summation index "fin" describes the complete relaxation channel given by continuum solution (LM) and bound part ($|\tilde\psi_{\text{fin}}\rangle$).

III. COMPUTATIONAL DETAILS

A. Single center expansion

Dunning's *cc-pVTZ* basis set[34] was used to represent bound molecular orbitals (MOs) in all computations. For each ionization and Auger decay step, molecular orbitals were calculated by a restricted (open shell) Hartree Fock procedure (R(O)HF) optimized for the initial electronic state. Thus, we calculated MOs for the neutral and double core ionized state by RHF, respectively, and MOs for the single core ionized state with ROHF. The self-consistent field optimization for core ionized states was carried using a modified PSI3 quantum package[35] as described elsewhere.[36] This procedure is known to account for most of the core electron vacancy induced orbital relaxation effects.[37]

From the resulting MOs, the SCE of each orbital $\phi^i(\mathbf{r})$ (Eq. (6)) has the radial parts

$$P_{lm}^i(r) = r \int d\Omega\, \phi^i(\mathbf{r}) Y_{lm}^*(\theta,\phi). \quad (31)$$

These radial parts as well as the radial parts of their electrostatic potential and density were numerically calculated using Gaussian-Legendre integration with 20×20 integration points in angle space. Because all of these quantities are real, real valued *tesseral* spherical harmonics[38] instead of the usual complex valued spherical harmonics were used to reduce the computational cost. Angular integrals over three spherical harmonics, also known as Gaunt coefficients, are readily calculated by evaluation of Wigner $3 - j$ symbols.[39]

For the radial coordinate non-equidistant radial grid points r were used[21] implicitly determined by

$$\rho(r) = \alpha r + \beta \ln r + \sum_n \arctan\frac{r - R_n}{\gamma}. \quad (32)$$

Here R_n are the distances of atom n to the center of the expansion, and variable ρ is discretized on an equidistant grid. The number of radial grid points was 1500, the largest radial grid point was set to $r = 20$ a.u., and the center for the expansion was chosen at the position of the oxygen atom, which allowed the SCE to limit to angular quantum numbers $l \leq 5$,

resulting in 36 different (*lm*) tuples. These parameters turned out to represent the molecular orbitals and relevant continuum wavefunctions of the water molecule sufficiently accurate and thus have been used for all subsequent calculations.

B. Configurational mixing

We applied the *frozen orbital approximation*, i.e., initial and final electronic states were represented by the same orbital set. In particular, orbitals optimized for the initial state by the R(O)HF calculation mentioned above were used. The molecular orbital integrals, obtained from the PSI3 quantum package,[35] were used to perform spin adapted multi-reference configuration interaction (MRCI) calculations for the final bound electronic states $|\tilde{\psi}_{\mathrm{fin},M_S}^S\rangle$ and single reference configuration interaction (CI) calculations[40] for the initial states $|\tilde{\psi}_{\mathrm{ini},M_S}^S\rangle$. As references for the final state we have chosen the initial state reference with all possible combinations of one additional vacancy (for photoionization) or two valence electrons removed and a re-occupied core orbital (for Auger decay). From the reference occupations configuration state functions (CSFs) were built considering single excitations within the full MOs space and double excitations up to the 20th MO. This truncation of the CI space was used for both single and the multi-reference calculations, leading to a number of 2297–5852 CSFs for the initial states (single reference CI) and 8125–18220 CSFs for the final state (MRCI). From these calculations only solution vectors with significant contributions in the references (norm of projection into reference subspace >0.01) were used for subsequent calculations. For these solution vectors the SCE of the electrostatic potential and the electron density of the respective final electronic state was obtained as a linear combination of the electrostatic potential and electron density of the MOs.

C. Integration of the continuum wavefunction

For the relevant CI vectors, the 36 solutions for the continuum wavefunctions in the potential of the molecule of the specific final electronic state $|\tilde{\psi}_{\mathrm{fin},M_S}^S\rangle$ were integrated according to Eq. (7) for the given boundary conditions (Eq. (17)) using the *vector sweep* integration method adopted from Ref. 21. The continuum normalization was carried out by diagonalizing the obtained **R** matrix as described by Eq. (18).

D. Transitions

Photoionization cross sections and Auger decay transition rates were calculated by evaluating Eqs. (21) and (25) using Simpson's rule. In particular, for the two electron integrals a system of coupled differential equations[21,41] was solved for $r \cdot y_{lm}^{ik}(r)$ and then Eq. (28) was integrated by Simpson's rule, as had been described for atoms.[42] As different angular continuum channels were not distinguished here, transition rates for different continuum solutions (*LM*) were finally summed up.
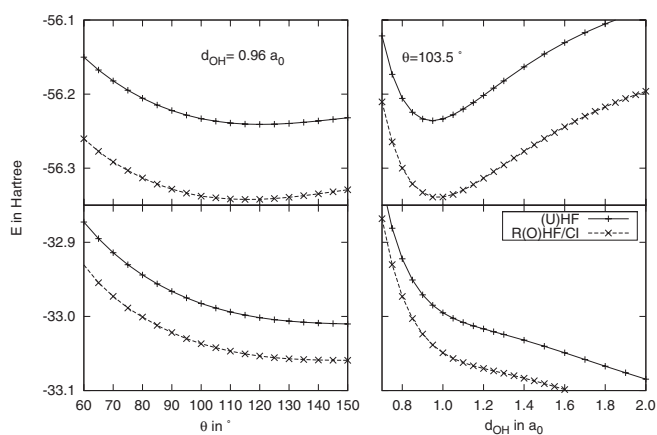

FIG. 1. Cuts through the potential energy surfaces for single (top) and double core (bottom) ionized water. (Left) Both hydrogen atoms are at equilibrium distance $d_{\mathrm{OH}} = 0.96a_0$ to the oxygen for different HOH angles Θ. (Right) One hydrogen atom is fixed at $d_{\mathrm{OH}} = 0.96a_0$ and the other is at variable distances to the oxygen atom, while Θ is at equilibrium value of $103.5°$.

E. Molecular dynamics calculations

All calculations of Auger decay rates were performed for a set of molecular geometries, obtained by *ab initio* molecular dynamics (MD) simulation. The nuclei were propagated using the Beeman integration scheme[43] with a 0.1 fs time step in the single and double core ionized state. Energy gradients were calculated with GAUSSIAN 09 (Ref. 44) from unrestricted Hartree Fock (UHF) calculations for the single core ionized state and restricted Hartree Fock (RHF) calculations for the double core ionized state. Convergence of the self-consistent field procedure to the desired open core shell states was achieved by choosing an initial guess based on neutral optimized orbitals with single or unoccupied core orbital, respectively. To assess the accuracy of the (U)HF method used to generate the trajectories, we compared two sections of the potential energy surface obtained by the single determinant (U)HF method with that obtained by the CI method described in Sec. II B. As seen in Fig. 1, very similar curves are obtained, apart from a nearly constant offset. Therefore, we consider the gradients at (U)HF level to be sufficiently accurate to describe the nuclear dynamics after core ionizations.

F. Initial conditions

The Auger spectrum of water is dominated by Franck-Condon broadening due to the very steep potential energy surfaces of the final electronic states. To estimate this broadening (as described further below), multiple MD trajectories were calculated with initial conditions at the 1σ standard deviation of the ground state Wigner distribution. To that aim, neutral ground state optimization and vibrational mode calculations[40] using harmonic approximation were performed with GAUSSIAN 09 (Ref. 44) on the MP2 level. From the optimized ground state geometry six different initial conditions with zero velocities were generated by varying the geometry in positive and negative directions along each of the three normal modes by the standard deviation σ of the vibrational ground state distribution. Six further initial conditions were

generated from the optimized geometry with initial velocities in positive and negative directions along the vibrational normal modes. These velocities were chosen to match the standard deviation σ of the vibrational ground state velocity distribution. Together with the optimized geometry with zero velocity, a total set of 13 sets of initial conditions were thus obtained.

G. Spectrum

For each of the 13 initial conditions, molecular dynamics simulations in the single core ionized state were started. Rather than estimating the Franck Condon broadening of the Auger lines from a weighted average over many Wigner-distributed trajectories (which would require a considerable number of trajectories to achieve sufficient sampling), the variance of the assumed Gaussian line profile of the dominant Auger transitions was estimated from the differences $\Delta\epsilon(t)$ in the Auger transition energies between the "central" trajectory (started from the optimized geometry with zero initial velocities) and the 12 "satellite" trajectories (started from altered initial conditions) as

$$\sigma^2(t) = \sigma_{\exp}^2 + \sigma_{\text{lifetime}}^2 + \sum_{i=1}^{3} \frac{\Delta\epsilon_{i,+x}^2(t) + \Delta\epsilon_{i,-x}^2(t)}{2}$$
$$+ \frac{\Delta\epsilon_{i,+v}^2(t) + \Delta\epsilon_{i,-v}^2(t)}{2}. \tag{33}$$

This computationally more efficient estimate rests on the assumption that the Gaussian shape of the nuclei wave packet is approximately maintained during the short simulation time. More precisely, we assume that the peak of the wave-packet remains sufficiently close to the "central" trajectory, and the "satellite" trajectories remain *on average* sufficiently close to the surrounding 1σ hypersurface, such that the width of the wave packet can be estimated from their average distance to the "central" trajectory. Additionally, we assume that within the phase space region covered by the wave packet, the transition energy is sufficiently linear in the atomic coordinates and the individual transition rates are constant. Visual inspection of the trajectories showed that these conditions are satisfied. This allowed us to restrict the computation of Auger transition rates to the "central" trajectory, while for the "satellite" trajectories only transition energies needed to be calculated.

In Eq. (33) $\Delta\epsilon_{i,\pm x}(t)$ denotes the difference of the transition energy between the "central" and the "satellite" trajectory, started with geometries modified along the vibrational mode i. Similarly, $\Delta\epsilon_{i,\pm v}(t)$ denotes the difference of the transition energy between the "central" and the "satellite" trajectory, started with velocities modified along vibrational mode i. Additionally, the effect due to limited experimental resolution and due to line broadening was included, with $\sigma_{\exp}$ = 0.17 eV (0.4 eV FWHM (Ref. 45)), and σ_{lifetime} estimated from the decay rates calculated in Sec. IV B.

To follow the evolution of double core ionized water after a period of nuclear dynamics in the single core ionized state, additional simulations of the double core ionized state
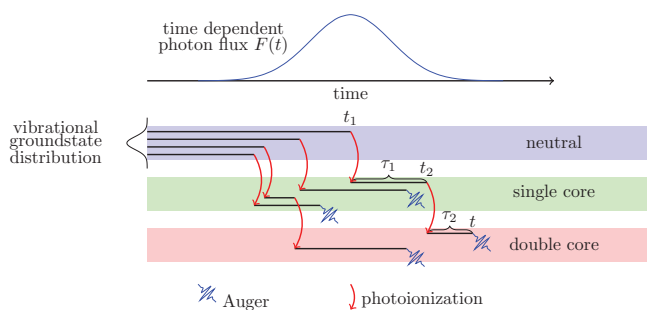

FIG. 2. Illustration of different ionization pathways. The total Auger spectrum is obtained from a superposition of spectra resulting from different trajectories along the neutral, single core ionized, and double core ionized states. Here, as an example, 4 pathways contributing to the single and the double core Auger spectrum are illustrated.

were started from selected snapshots of the single core ionized state trajectories ("central" and "satellite") at 0, 1, ... 9 fs, thus resulting in a total of 130 double core trajectories. The simulation time for each of the concatenated single and double core trajectories was limited to 10 fs, and the simulation time in the double core ionized state was limited to 7 fs.

Figure 2 illustrates how the spectra were composed of different trajectories using different pathways through the single and double core ionized states. The accumulated single and double core hole Auger spectra, S_1 and S_2, were calculated considering all possible pathways by

$$S_1 = \int_{-\infty}^{\infty} dt \int_{-\infty}^{t} dt_1 \, p_1(t, t_1) \, s_1(t - t_1), \tag{34}$$

$$S_2 = \int_{-\infty}^{\infty} dt \int_{-\infty}^{t} dt_2 \int_{-\infty}^{t_2} dt_1 \, p_2(t, t_1, t_2) \, s_2(t - t_1, t - t_1 - t_2),$$
$$\tag{35}$$

where $s_1(\tau_1)$ is the time-dependent single core Auger spectrum obtained as instantaneous spectrum from the geometry resulting from propagating nuclei in the single core ionized state for a time interval τ_1. Similarly, $s_2(\tau_1, \tau_2)$ denotes the instantaneous double core Auger spectrum resulting after a time interval τ_1 of nuclear dynamics in the single core ionized state and subsequent nuclear dynamics in the double core ionized state for an interval τ_2. The instantaneous single core Auger spectra $s_1(\tau_1)$ were weighted here with the joint probability $p_1(t, t_1) \, dt_1$ of finding the molecule at time t in the single core ionized state after ionization at time t_1. Similarly the double core Auger spectra $s_2(\tau_1, \tau_2)$ were weighted with the joint probability $p_2(t, t_1, t_2) \, dt_1 dt_2$ of finding the molecule in double core ionized state given that the first and second ionizations have occurred at times t_1 and t_2, respectively.

The joint probability densities $p_1(t, t_1)$ and $p_2(t, t_1, t_2)$ are expressed in terms of conditional probabilities $p_1(t|t_1)$ and $p_2(t|t_1, t_2)$ by

$$p_1(t, t_1) = p_1(t|t_1) \, p_0(t_1) \sigma_{0 \to 1} F(t_1), \tag{36}$$

$$p_2(t, t_1, t_2) = p_2(t|t_1, t_2) \, p_1(t_2, t_1) \sigma_{1 \to 2} F(t_2), \tag{37}$$

where $p_0(t)$ is the probability of the neutral electronic state at time t, $F(t)$ is the photon flux, and $\sigma_{i \to j}$ are the partial

photoionization cross sections. Here the indices 0, 1, and 2 denote the neutral, single core ionized, and double core ionized states, respectively. The conditional probabilities were obtained from the numerical solution of the master equations

$$\frac{dp_0(t)}{dt} = -p_0(t)\sigma_0 F(t); \quad p_0(t \to -\infty) = 1, \quad (38)$$

$$\frac{dp_1(t|t_1)}{dt} = -p_1(t|t_1)\left(\Gamma_1^{\text{Auger}} + \sigma_1 F(t)\right); \quad p_1(t_1|t_1) = 1,$$

$$(39)$$

$$\frac{dp_2(t|t_1, t_2)}{dt} = -p_2(t, |t_1, t_2)\Gamma_2^{\text{Auger}}; \quad p_2(t_2, |t_1, t_2) = 1.$$

$$(40)$$

Here we neglected any geometry (i.e., time) dependence of the total Auger decay rates Γ_1^{Auger} and Γ_2^{Auger} as well as of the respective photoionization cross sections $\sigma_{i \to j}$, because they all were found to vary by less than 2% for all obtained geometries. To gain more insight in the ionization process, also the *total* populations of the single and double core ionized state at time t were considered, given by

$$N_1(t) = \int_{-\infty}^{t} dt_1 \; p_1(t, t_1) \quad (41)$$

$$N_2(t) = \int_{-\infty}^{t} dt_2 \int_{-\infty}^{t_2} dt_1 \; p_2(t, t_1, t_2). \quad (42)$$

H. Illumination conditions

We assumed a Gaussian x-ray pulse with 10 fs FWHM. Soft x-ray photon beams at photon energies of 1 keV were considered, with peak intensities of 10 photons/fs $\text{Å}^2 \simeq 1.6 \times 10^{16}$ W/cm², 100 photons/fs $\text{Å}^2 \simeq 1.6 \times 10^{17}$ W/cm², and 1000 photons/fs $\text{Å}^2 \simeq 1.6 \times 10^{18}$ W/cm², respectively. These parameters agree with the regime offered by the Atomic, Molecular and Optical science instrument at the LCLS (Ref. 46) and provide a high ionization rate such that a considerable amount of double core ionizations is reached.

For visible light one might argue that such high fluxes give rise to instantaneous multi-photon ionization or tunnel ionization events. These effects are relevant if the ponderomotive energy $U_p = \frac{8\pi}{137} \frac{I}{4\omega^2}$ exceeds the ionization energy. However, for the x-ray pulses considered here, $U_p \leq 0.14$ eV, which is far below the ionization energy. Despite the high intensities, these effects can therefore assumed to be negligible, and thus the perturbative approach of sequential photoionization is justified.

IV. RESULTS AND DISCUSSION

A. Photoionization cross sections

We first tested our approach by comparing calculated total photoionization cross sections for neon with values from McMasters compilation of x-ray cross sections[47] for selected

TABLE I. Calculated total photoionization cross sections for atomic neon compared to values from Ref. 47.

Photon energy (keV)	This work in 10^{-3} a.u.	From McMaster *et al.* [47] in 10^{-3} a.u.
1	9.63	9.10
2	1.53	1.51
10	0.0137	0.0137

photon energies. As shown in Table I, our calculated ionization cross sections agree well with the tabulated values. Table II lists the obtained total and partial cross sections of water for a photon energy of $\omega = 1$ keV. For water, the ratio of the partial cross sections to the single core ionized state to the total cross section $\sigma_{0 \to 1}/\sigma_0$ is about 80%. The remaining 20% mostly involve core ionization with additional shake-up transitions of valence electrons. A similar ratio is seen for the second ionization step.

B. Auger decay rates

To also validate Auger decay rate calculations, we compared in Table III calculations for neon with calculations from Kolorenč and Averbukh,[48] Bhalla *et al.*,[49] Yarzhemsky and Sgamellotti[50] (single core), Kelly[51] (single core), Pelicon *et al.*[52] (double core), and Chen[53] (double core). The values reported in these studies vary by about 10% for the single core and by up to 20% for the double core Auger transition. As can be seen in Table III, our values fall within these ranges.

Table IV compares the calculated single core Auger transition rates for water with previous calculations of absolute[15] and relative values.[26] We have adjusted the calculated energies to the experimental spectrum (see Fig. 5) by subtracting an overall offset of 1.1 eV. This offset may result from neglecting relativistic effects in our calculation, truncation of the CI space, or incomplete basis sets.

As can be seen, the relative rates (normalized to the dominant $1b_1^{-2}$ S peak) compare well in the higher energy regime, where final states consist of two outer valence holes. In the lower energy range, somewhat larger deviations are seen, which can be explained by the stronger influence of shake-up contributions. Notably, our values tend to be larger than the Auger decay rates obtained by Stieltjes imaging calculations by Carravetta and Ågren[15] and Kolorenč and Averbukh,[48] with a total transition rate of 6.0×10^{-3} a.u. compared to

TABLE II. Calculated total and partial photoionization cross sections for water at 1 keV. The indices 0, 1, and 2 denote the neutral, single core ionized, and double core ionized state, respectively.

Transition	Cross section in 10^{-3} a.u.
σ_0	3.84
$\sigma_{0 \to 1}$	3.08
σ_1	2.62
$\sigma_{1 \to 2}$	2.17

TABLE III. Comparison of calculated Auger decay rates for singly and doubly core ionized neon in 10^{-3} a.u.

		Total single core Auger decay rate in 10^{-3} a.u.			
This work	Kolorenč and Averbukh[48]	Yarzhemsky and Sgamellotti[50]	Kelly[51]	Bhalla *et al.*[49]	
9.9	9.2	8.9	8.1	8.8	
		Total double core Auger decay rate in 10^{-3} a.u.			
This work	Kolorenč and Averbukh[48]	Pelicon *et al.*[52]	Chen[53]	Bhalla *et al.*[49]	
26.1	18.6	22.9	29.5	26.0	

5.5×10^{-3} a.u. (Ref. 15) and 5.4×10^{-3} a.u. (Ref. 48). However, our value for the total Auger decay rate is similar to the single core hole decay rate measured by Sankari *et al.*,[54] $5.8 \pm 0.2 \times 10^{-3}$ a.u.

   Table V shows transition rates obtained for the double core Auger spectrum of water. As for the single core Auger transitions, energies have been shifted by 1.1 eV. We note, however, that relativistic contributions not taken into account in our calculations may contribute about $\simeq$1–2 eV more in the double than in the single core hole case.[55] The obtained total double core decay rate (18.2×10^{-3} a.u.) is about three times larger than the single core decay rate. It is also significantly larger than the value reported by Kolorenč and Averbukh[48] who used Stieltjes imaging method (11.4×10^{-3} a.u.). These authors[48] estimated their value to be 20% too low due to insufficient inclusion of initial state orbital relaxation effects. This estimation was based on the discrepancy between their results and other calculations for atomic neon (see Table III). Whereas Kolorenč and Averbukh[48] used neutral state opti-

TABLE V. Total Γ_2^{Auger} and partial $\Gamma_{2 \to f}^{Auger}$ Auger transition rates of water (double core) for the main transition channels (MP2 optimized equilibrium geometry).

Channel	Energy in eV	$\Gamma_{ini \to fin}^{Auger}$ in 10^{-4} a.u.
$1b_1^{-2}$	556.13	24.70
$3a_1^{-1}1b_1^{-1}$	555.31	23.89
$1b_2^{-1}1b_1^{-1}$	552.81	18.18
$3a_1^{-2}$	552.35	19.11
$3a_1^{-1}1b_2^{-1}$	551.27	13.91
$1b_2^{-2}$	546.79	15.58
$2a_1^{-1}1b_1^{-1}$	532.02	13.42
$2a_1^{-1}3a_1^{-1}$	531.53	13.78
$2a_1^{-1}1b_2^{-1}$	527.35	9.37
$2a_1^{-2}$	513.27	7.65
Γ_2^{Auger}		182.3

mized orbitals and cover orbital relaxation effects in initial and final states with the ADC(2)x (Ref. 56) method, our calculation is based on initial state optimized orbitals and incorporates final state orbital relaxation by configurational interaction. We therefore assume that our calculation does not suffer from these problems.

C. Population

   Figure 3 shows the populations of the neutral, single, and double core ionized states obtained from Eqs. (41) and (42) for different beam intensities. The decrease rate of the neutral population increases with pulse intensity, whereas the transition rate to single and double core ionized populations

TABLE IV. Total Γ_1^{Auger} and partial $\Gamma_{1 \to fin}^{Auger}$ Auger transition rates of water (single core) for the main transition channels (MP2 optimized geometry) compared to calculations from Carravetta and Ågren [15] and Siegbahn *et al.*[26]

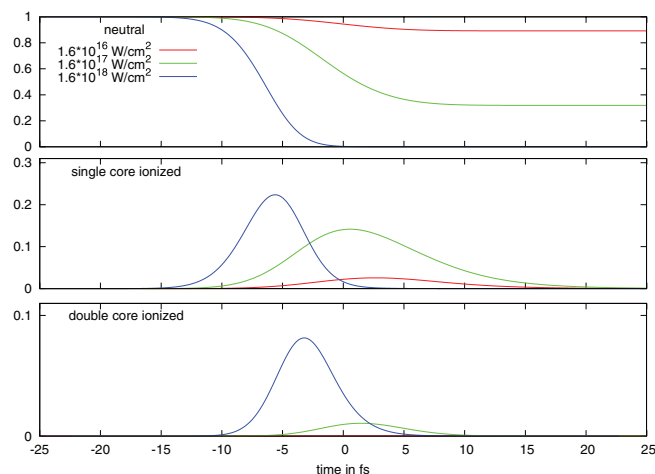|	Energy in eV	$\Gamma_{ini \to fin}^{Auger}$ in 10^{-4} a.u.		Relative $\Gamma_{ini \to fin}^{Auger}$		
Channel	This work	This work	From Ref. 15	This work	From Ref. 15	From Ref. 26
$3a_1^{-1}1b_1^{-1}$ T	500.67	0.26	0.11	3	2	2
$1b_1^{-2}$ S	499.39	8.25	5.79	100	100	100
$3a_1^{-1}1b_2^{-1}$ S	497.98	7.59	5.57	92	96	99
$1b_2^{-1}1b_1^{-1}$ T	496.60	0.00	0.00	0	0	0
$1b_2^{-1}1b_1^{-1}$ S	494.68	6.57	5.33	80	92	74
$3a_1^{-2}$ S	494.64	5.74	3.93	70	68	71
$3a_1^{-1}1b_2^{-1}$ T	494.63	0.20	0.09	2	2	1
$3a_1^{-1}1b_2^{-1}$ S	492.36	5.62	5.57	68	96	58
$1b_2^{-2}$ S	487.45	4.55	3.45	55	60	34
$2a_1^{-1}1b_1^{-1}$ T	482.30	2.03	1.19	25	21	14
$2a_1^{-1}3a_1^{-1}$ T	480.58	1.78	1.66	22	29	11
$2a_1^{-1}1b_2^{-1}$ T	476.82	1.02	1.19	12	21	8
$2a_1^{-1}1b_1^{-1}$ S	475.76	3.19	3.35	39	58	55
$2a_1^{-1}3a_1^{-1}$ S	473.27	3.86	3.74	47	65	48
$2a_1^{-1}1b_2^{-1}$ S	468.75	2.18	2.58	26	45	32
$2a_1^{-2}$ S	457.19	1.51	3.54	18	61	48
Γ_1^{Auger}		60.01	55.20			

FIG. 3. Integrated population of the neutral $N_0(t)$, single core ionized $N_1(t)$, and double core ionized states $N_2(t)$. A Gaussian shaped x-ray pulse centered at time $t = 0$ fs, width of 10 fs FWHM and a photon energy of 1 keV was assumed.

increase, such that their peak positions are shifted to earlier times.

As can be seen in Table VI, the probability for double core ionization is about 100 times smaller than for single core ionization at 1.6×10^{16} W/cm^2, and reaches a ratio of 0.465 at 1.6×10^{18} W/cm^2. At 1.6×10^{18} W/cm^2 the first ionization step is saturated, and the probability of first core ionization agrees with the ratio $\sigma_{0\rightarrow1}/\sigma_0 = 0.802$. Note that the missing 20% from shake-up contributions and valence ionizations are not considered here and thus are missing in our simulations. After Auger decay the molecule may undergo further core ionizations, as has been observed for Neon.[10] Note that these further ionization steps, which involve a large number of different channels, are not included in our simulation.

D. Single and double core ionized Auger spectra

Figure 4 illustrates trajectories starting from zero velocities and equilibrium geometry by snapshots of the electron densities in the molecular plane, calculated from the CI wavefunctions. The evolution of the OH bond length is shown in the upper left panel, that of the HOH bond angle in the supplementary material.[40] As can be seen, in the single core ionized state the nuclei motion is mainly a bending motion, whereas in the double core ionized state protons are rapidly expelled from the molecule within a few femtoseconds. During that process, and with further ionization, the electron density becomes increasingly isotropic.

TABLE VI. Total probability of single and double core ionization for different flux intensities.

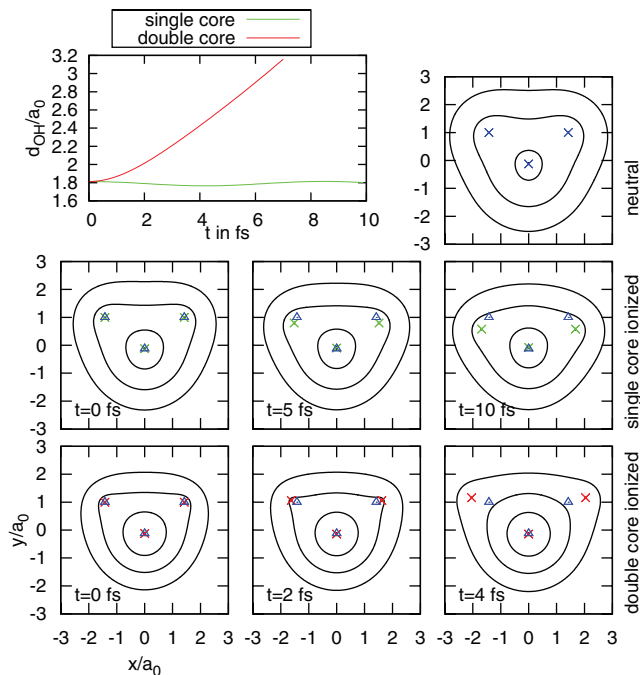| Intensity (W/cm^2)	1st core ionization	2nd core ionization	Ratio 2nd/1st
1.6×10^{16}	0.087	0.001	0.01
1.6×10^{17}	0.546	0.069	0.13
1.6×10^{18}	0.802	0.373	0.465

FIG. 4. Dynamics of a water molecule after single (middle row) and double (bottom row) core ionization. The upper left plot shows the evolution of the OH-bond length d_{OH} for the single and double core ionized state. The other plots show cuts through the electron density in the molecular plane (contour lines) at three selected times for the neutral, single core ionized, and double core ionized state. Crosses denote the positions of the nuclei; triangles mark the neutral equilibrium positions of the nuclei. All plots refer to the trajectory starting from equilibrium geometry with zero initial velocities.

Figure 5 compares the calculated single core spectrum at peak intensity 1.6×10^{16} W/cm^2 with the spectrum measured by Moddeman *et al.*[45] Also shown for comparison are the calculated spectra obtained with frozen nuclei. As can be seen, the calculated spectrum captures most of the features of the experimental spectrum very well. Only small deviations to the spectrum with frozen nuclei are observed. Obviously, for single core ionization the influence of the nuclear motion
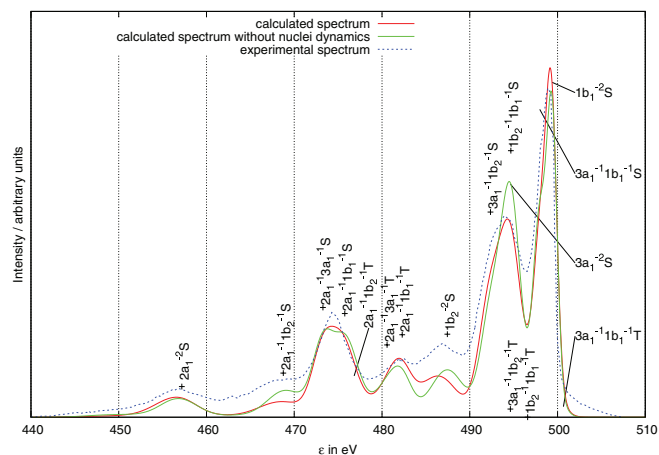

FIG. 5. Single core Auger spectrum. Comparison of experimental spectrum[45] (dashed line) and calculated spectrum for peak intensity $I = 1.6 \times 10^{16}$ W/cm^2 with (red line) and without (green line) nuclei dynamics. The position of the peaks were labeled according to their dominant hole configurations.
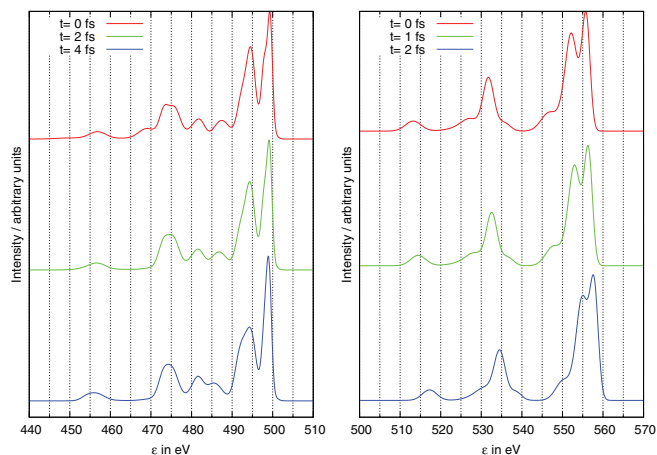
FIG. 6. (Left) Instantaneous single core Auger spectra after 0 fs, 2 fs, and 4 fs of the single core ionized state. (Right) Instantaneous double core Auger spectra after 0 fs, 1 fs, and 2 fs of the double core ionized state. For the double core Auger spectrum, nuclear motion was calculated only for the double core ionized state. The fast dissociation in the double core ionized state is reflected by the fast shift of the Auger spectrum to higher energies.

FIG. 8. Single and double core Auger spectrum for different peak intensities. At peak intensity 1.6×10^{18} W/cm^2 the two parts of the Auger spectrum are at comparable intensity.

in the Auger spectrum is rather small, which can also be seen in Fig. 6 (left), where a set of instantaneous Auger spectra of selected snapshots of the single core ionized state trajectories are shown. Indeed, for different times these Auger spectra are very similar, with the notable exception at about 485–495 eV, where final states are associated with vacancies in outer valence orbitals $1b_2$ and $3a_1$, which are mostly affected by the hydrogen bending movement and thus sensitive to small geometry changes. The valence orbital $1b_1$ is only weakly affected by geometry changes as its nodal plane is identical with the molecular plane.

Figure 7 shows the calculated double core spectrum at peak intensity 1.6×10^{18} W/cm^2 and the calculated spectrum with frozen nuclei. Here the nuclear dynamics causes a long tail to higher energies for each peak in the spectrum. The instantaneous spectra at different time steps (Fig. 6, right) confirm that the spectra indeed shift to higher energies as the
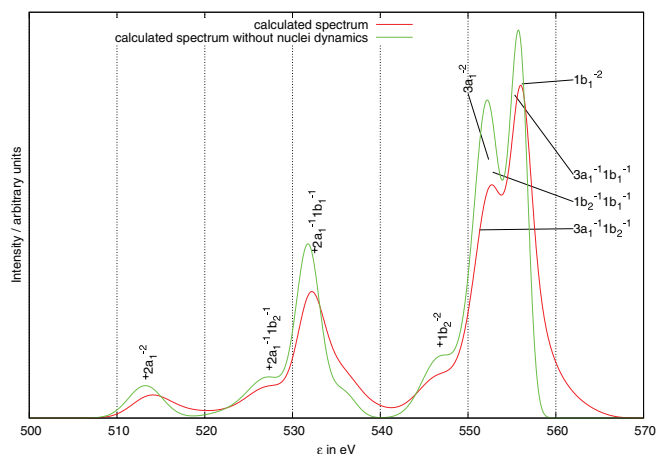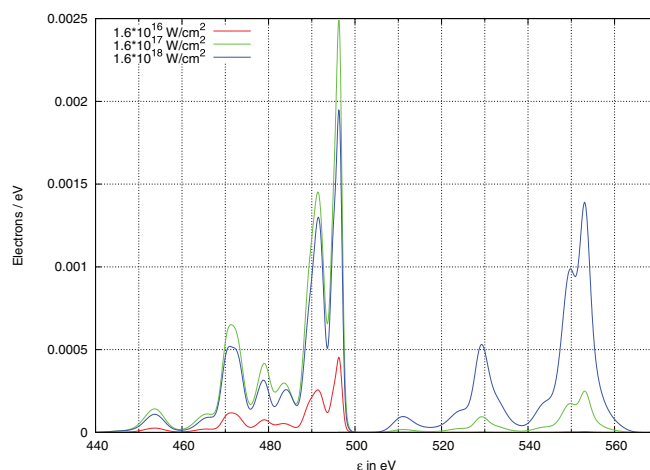
double core ionized state evolves. This is a result of the strong dissociative motion in the double core ionized state (see Fig. 4, bottom). As both protons are repelled, positive charge is removed from the molecule. As a result, the subsequent Auger recombination involves larger energy differences.

The combined single and double core Auger spectra, composed according to Eqs. (34) and (35), are shown in Fig. 8 for the same flux parameters as in Fig. 3. For 1.6×10^{16} W/cm^2 the single core Auger spectrum clearly dominates, while at 1.6×10^{17} W/cm^2 the double core spectrum has already significant contribution. At peak intensity 1.6×10^{18} W/cm^2, the double core and single core spectra reach the same intensity. Here, about 50% of the population is double core ionized, such that the single core Auger spectrum becomes even smaller than for 1.6×10^{17} W/cm^2.

V. CONCLUSION

We have developed a procedure for calculating *ab initio* transition rates for photoionization and molecular Auger decay, which was validated against previous calculations and experimental data for neon. Our test calculations demonstrates that the single center expansion method in combination with LCAO for the bound MOs provides reliable cross sections and transition rates for water. It was demonstrated that for describing ionization dynamics the second core ionization process must be considered for intensities above 10^{17} W/cm^2.

Auger spectra were computed for a single and double core ionized water molecule. For these calculations, the nuclear dynamics during the core hole lifetime were described by an MD approach based on the core ionized UHF/RHF wavefunction. The obtained total Auger decay rates as well as the spectra agree well with previous experimental data. Strikingly, the Auger decay rate of double core ionized water turned out to be three times larger than that of single core ionized water. Only small effects of the nuclear motion on the single core Auger spectrum were seen. In contrast, for the double core ionized water molecule fast dissociation dynamics is seen, which

FIG. 7. Double core Auger spectrum. Calculated spectrum for peak intensity $I = 1.6 \times 10^{18}$ W/cm^2 with (red line) and without (green line) nuclei dynamics. The positions of the peaks are labeled according to their dominant hole configurations.

strongly affects the respective Auger spectra. A particular signature of nuclear motion, which should be seen in future FEL experiments, are marked tails at the higher energy side of most peaks. This signature, therefore, might provide an independent probe for detecting fast nuclear motion on femtosecond time scales. Future work should address possible vibrational interference effects for the nuclear motion, which in our incoherent accumulation of spectra have been neglected. Although only small interference effects are expected for the single core hole Auger spectrum of the water monomer, more pronounced fingerprints might be visible in the double core hole Auger spectrum, and in particular in the spectra of the water dimer as has been demonstrated for the x-ray emission spectrum.[57,58]

ACKNOWLEDGMENTS

[1]R. Neutze, R. Wouts, D. van der Spoel, E. Weckert, and J. Hajdu, "Potential for biomolecular imaging with femtosecond X-ray pulses," Nature (London) **406**, 752 (2000).

[2]K. J. Gaffney and H. N. Chapman, "Imaging atomic structure and dynamics with ultrafast X-ray scattering," Science **316**, 1444 (2007).

[3]M. Makris, P. Lambropoulos, and A. Mihelič, "Theory of multiphoton multielectron ionization of xenon under strong 93-eV radiation," Phys. Rev. Lett. **102**, 33002 (2009).

[4]N. Rohringer and R. Santra, "X-ray nonlinear optical processes using a self-amplified spontaneous emission free-electron laser," Phys. Rev. A **76**, 033416 (2007).

[5]S. Son, L. Young, and R. Santra, "Impact of hollow-atom formation on coherent x-ray scattering at high intensity," Phys. Rev. A **83**, 033402 (2011).

[6]R. Santra, N. V. Kryzhevoi, and L. S. Cederbaum, "X-ray two-photon photoelectron spectroscopy: a theoretical study of inner-shell spectra of the organic para-aminophenol molecule," Phys. Rev. Lett. **103**, 013002 (2009).

[7]M. Tashiro, M. Ehara, H. Fukuzawa, K. Ueda, C. Buth, N. V. Kryzhevoi, and L. S. Cederbaum, "Molecular double core hole electron spectroscopy for chemical analysis," J. Chem. Phys. **132**, 184302 (2010).

[8]L. S. Cederbaum, F. Tarantelli, A. Sgamellotti, and J. Schirmer, "On double vacancies in the core," J. Chem. Phys. **85**, 6513 (1986).

[9]J. H. D. Eland, M. Tashiro, P. Linusson, M. Ehara, K. Ueda, and R. Feifel, "Double core hole creation and subsequent auger decay in nh$_3$ and ch$_4$ molecules," Phys. Rev. Lett. **105**, 213005 (2010).

[10]L. Young, E. P. Kanter, B. Kraessig, Y. Li, A. M. March, S. T. Pratt, R. Santra, S. H. Southworth, N. Rohringer, L. F. DiMauro, G. Doumy, C. A. Roedig, N. Berrah, L. Fang, M. Hoener, P. H. Bucksbaum, J. P. Cryan, S. Ghimire, J. M. Glownia, D. A. Reis, J. D. Bozek, C. Bostedt, and M. Messerschmidt, "Femtosecond electronic response of atoms to ultra-intense X-rays," Nature (London) **466**, 56 (2010).

[11]L. Fang, M. Hoener, O. Gessner, F. Tarantelli, S. T. Pratt, O. Kornilov, C. Buth, M. Guehr, E. P. Kanter, C. Bostedt, J. D. Bozek, P. H. Bucksbaum, M. Chen, R. Coffee, J. Cryan, M. Glownia, E. Kukk, S. R. Leone, and N. Berrah, "Double core-hole production in N-2: beating the Auger clock," Phys. Rev. Lett. **105**, 083005 (2010).

[12]C. Gnodtke, U. Saalmann, and J. M. Rost, "Ionization and charge migration through strong internal fields in clusters exposed to intense x-ray pulses," Phys. Rev. A **79**, 041201 (2009).

[13]Z. Jurek and G. Faigel, "The effect of tamper layer on the explosion dynamics of atom clusters," Eur. Phys. J. D **50**, 35 (2008).

[14]Z. Jurek and G. Faigel, "The effect of inhomogenities on single-molecule imaging by hard XFEL pulses," EPL **86**, 68003 (2009).

[15]V. Carravetta and H. Ågren, "Stieltjes imaging method for molecular auger transition rates - application to the auger spectrum of water," Phys. Rev. A **35**, 1022 (1987).

[16]B. Schimmelpfennig, B. Nestmann, and S. Peyerimhoff, "Ab initio calculation of transition rates for autoionization: the Auger spectra of HF and F$^-$," J. Electron Spectrosc. Relat. Phenom. **74**, 173 (1995).

[17]R. Colle and S. Simonucci, "Method for calculating Auger decay-rates in molecules," Phys. Rev. A **39**, 6247 (1989).

[18]E. Chelkowska and F. Larkins, "Auger-Spectroscopy for molecules—tables of matrix-elements for transition-rate calculations corresponding to an s-type, p-type, or d-type initial hole," At. Data Nucl. Data Tables **49**, 121 (1991).

[19]M. Mitani, O. Takahashi, K. Saito, and S. Iwata, "Theoretical molecular Auger spectra with electron population analysis," J. Electron Spectrosc. Relat. Phenom. **128**, 103 (2003).

[20]M. Tashiro, K. Ueda, and M. Ehara, "Auger decay of molecular double core-hole state," J. Chem. Phys. **135**, 154307 (2011).

[21]P. Demekhin, A. Ehresmann, and V. Sukhorukov, "Single center method: a computational tool for ionization and electronic excitation studies of molecules," J. Chem. Phys. **134**, 024113 (2011).

[22]M. Odelius, "Molecular dynamics simulations of fine structure in oxygen *K*-edge x-ray emission spectra of liquid water and ice," Phys. Rev. B **79**, 144204 (2009).

[23]O. Takahashi, M. Odelius, D. Nordlund, A. Nilsson, H. Bluhm, and L. Pettersson, "Auger decay calculations with core-hole excited-state molecular-dynamics simulations of water," J. Chem. Phys. **124**, 064307 (2006).

[24]M. Eroms, O. Vendrell, M. Jungen, H. Meyer, and L. Cederbaum, "Nuclear dynamics during the resonant Auger decay of water molecules," J. Chem. Phys. **130**, 154307 (2009).

[25]Z. Bao, R. Fink, O. Travnikova, D. Ceolin, S. Svensson, and M. Piancastelli, "Detailed theoretical and experimental description of normal Auger decay in O$_2$," J. Phys. B **41**, 125101 (2008).

[26]H. Siegbahn, L. Asplund, and P. Kelfve, "The Auger electron spectrum of water vapour," Chem. Phys. Lett. **35**, 330 (1975).

[27]R. Pauncz, *Spin Eigenfunctions: Construction and Use* (Plenum, New York, 1979).

[28]In cases where the total spin quantum numbers are irrelevant these additional indices are skipped in the notation.

[29]M. Deleuze, B. T. Pickup, and J. Delhalle, "Plane wave and orthogonalized plane wave many-body green's function calculations of photoionization intensities," Mol. Phys. **83**, 655 (1994).

[30]R. Gaspar, "Über eine approximation des Hartreefockschen potentials durch eine universelle potentialfunktion," Acta Phys. Acad. Sci. Hung. **3**, 263 (1954).

[31]P. Demekhin, D. Omelyanenko, B. Lagutin, V. Sukhorukov, L. Werner, A. Ehresmann, K.-H. Schartner, and H. Schmoranzer, "Investigation of photoionization and photodissociation of an oxygen molecule by the method of coupled differential equations," Opt. Spectrosc. **102**, 318 (2007).

[32]J. Sakurai and S. F. Tuan, *Modern Quantum Mechanics* (Benjamin/Cummings, 1985), Vol. 1.

[33]R. Manne and H. Ågren, "Auger transition amplitudes from general many-electron wavefunctions," Chem. Phys. **93**, 201 (1985).

[34]T. H. Dunning, "Gaussian basis sets for use in correlated molecular calculations. I. The atoms boron through neon and hydrogen," J. Chem. Phys. **90**, 1007 (1989).

[35]T. D. Crawford, C. D. Sherrill, E. F. Valeev, J. T. Fermann, R. A. King, M. L. Leininger, S. T. Brown, C. L. Janssen, E. T. Seidl, J. P. Kenny, and W. D. Allen, "PSI3: an open-source ab initio electronic structure package," J. Comp. Chem. **28**, 1610 (2007).

[36]P. S. Bagus, "Self-consistent-field wave functions for hole states of some Ne-like and Ar-like ions," Phys. Rev. **139**, A619 (1965).

[37]N. V. Kryzhevoi, R. Santra, and L. S. Cederbaum, "Inner-shell single and double ionization potentials of aminophenol isomers," J. Chem. Phys. **135**, 084302 (2011).

[38]E. Whittaker and G. Watson, *A Course of Modern Analysis* (Cambridge University Press, 1952).

[39]L. Biedenharn, J. Louck, and P. Carruthers, *Angular Momentum in Quantum Physics: Theory and Application*, Encyclopedia of Mathematics and its Applications Series, Vol. 8 (Addison-Wesley, Reading, 1981).

[40]See supplementary material at http://dx.doi.org/10.1063/1.3700233 for detailed results for initial state energies, the obtained ground state optimized geometry and vibrational mode frequencies, and the HOH bond angle evolution.

[41]L. Chernysheva, *Computation of Atomic Processes: A Handbook for the ATOM Programs*, Bd. 1 (Institute of Physics, 1997).

[42]J. McDougall, "The calculation of the terms of the optical spectrum of an atom with one series electron," Proc. R. Soc. Lond. Ser. A **138**, 550 (1932), see http://rspa.royalsocietypublishing.org/content/138/836/550.full.pdf+html.

[43]D. Frenkel and B. Smit, *Understanding Molecular Simulation* (Academic, San Diego, CA, 1996).

[44]M. J. Frisch, G. W. Trucks, H. B. Schlegel *et al.*, GAUSSIAN 09, Revision A.02 , Gaussian, Inc., Wallingford, CT, 2009.

[45]W. Moddeman, T. Carlson, M. Krause, B. Pullen, W. Bull, and G. K. Schweitz, "Determination of K-LL auger spectra of N_2, O_2, CO, NO, H_2O, and CO," J. Chem. Phys. **55**, 2317 (1971).

[46]SLAC National Accelerator Laboratory, "Atomic, molecular & optical science," 2012, see http://lcls.slac.stanford.edu/amo/.

[47]W. McMaster, N. del Grande, J. Mallett, and J. Hubbell, "Compilation of X-ray cross sections," Lawrence Radiation Laboratory Report No. UCRL-50174, Sec. II, Rev. 1 (1969).

[48]P. Kolorenč and V. Averbukh, "K-shell Auger lifetime variation in doubly ionized Ne and first row hydrides," J. Chem. Phys. **135**, 134314 (2011).

[49]C. P. Bhalla, N. O. Folland, and M. A. Hein, "Theoretical *K*-shell Auger rates, transition energies, and fluorescence yields for multiply ionized neon," Phys. Rev. A **8**, 649 (1973).

[50]V. Yarzhemsky and A. Sgamellotti, "Auger rates of second-row atoms calculated by many-body perturbation theory," J. Electron Spectrosc. Relat. Phenom. **125**, 13 (2002).

[51]H. P. Kelly, "*K* Auger rates calculated for Ne^+," Phys. Rev. A. **11**, 556 (1975).

[52]P. Pelicon, I. Čadež, M. Žitnik, Ž. Šmit, S. Dolenc, A. Mühleisen, and R. I. Hall, "Formation of the hollow $1s^{o1}S$ state of Ne^{2+} by electron impact: observation by means of an Auger hypersatellite," Phys. Rev. A **62**, 022704 (2000).

[53]M. H. Chen, "Auger transition rates and fluorescence yields for the double-*K* -hole state," Phys. Rev. A **44**, 239 (1991).

[54]R. Sankari, M. Ehara, H. Nakatsuji, Y. Senba, K. Hosokawa, H. Yoshida, A. D. Fanis, Y. Tamenori, S. Aksela, and K. Ueda, "Vibrationally resolved O 1s photoelectron spectrum of water," Chem. Phys. Lett. **380**, 647 (2003).

[55]J. Niskanen, P. Norman, H. Aksela, and H. Agren, "Relativistic contributions to single and double core electron ionization energies of noble gases," J. Chem. Phys. **135**, 054310 (2011).

[56]P. Kolorenč, V. Averbukh, K. Gokhberg, and L. S. Cederbaum, "Ab initio calculation of interatomic decay rates of excited doubly ionized states in clusters," J. Chem. Phys. **129**, 244102 (2008).

[57]M. P. Ljungberg, A. Nilsson, and L. G. M. Pettersson, "Semiclassical description of nuclear dynamics in x-ray emission of water," Phys. Rev. B **82**, 245115 (2010).

[58]M. P. Ljungberg, L. G. M. Pettersson, and A. Nilsson, "Vibrational interference effects in x-ray emission of a model water dimer: implications for the interpretation of the liquid spectrum," J. Chem. Phys. **134**, 044513 (2011).